Geomechanics and Engineering, *Vol. 18, No. 1 (2019) 1-9*
DOI: https://doi.org/10.12989/gae.2019.18.1.001

New 3D failure analysis of water-filled karst cave beneath deep tunnel

R. Zhang*[1,2] and X.L. Yang[1a]

[1]*School of Civil Engineering, Central South University, Hunan, 410075, China*
[2]*Department of Civil and Structural Engineering, University of Sheffield, U.K.*

(Received November 21, 2018, Revised March 25, 2019, Accepted April 3, 2019)

Abstract. In this study, both 2D and 3D failure shapes of rock mass above the water-filled cavity are put forward when the surrounding rock mass cannot bear the pressure caused by the water-filled cavity. Based on the analytical expressions derived by kinematic approach, the profiles of active and passive failure patterns are plotted. The sensitivity analysis is conducted to explore the influences of different rock parameters on the failure profiles. During the excavation of the deep tunnels above the karst cavity, the water table always changes because of progressive failure of cavity roof. Therefore, it is meaningful to discuss the effects of varying water level on the failure patterns of horizontal rock layers. The changing laws of the scope of the failure pattern obtained in this work show good consistency with the fact, which could be used to provide a guide in engineering.

Keywords: water-filled karst cavity; 3D failure mechanism; deep tunnel; pore-water pressure

1. Introduction

Recently, constructions for tunnels above the deep-buried karst cavity are growing in southwestern part of China. Because of geological conditions and historical reasons, the traffic infrastructures in southwest of China are still poor. The government is now encouraging investment in transportation development in the southwest of China: large numbers of railways and highways are under construction. In terms of the selection of highway route, straight lines are mostly used. In order to implement this design, a large number of tunnels are widely used, especially in water-rich mountainous regions. Many researches have focused on the stability of deep tunnel (Daraei and Zare 2018, Sahoo and Kumar 2018, Lin *et al.* 2018). Deep tunnels are located in areas with substantial heterogeneity of rock properties whose consideration is the state of the art in rock mechanics field, tunnelling, geo-energy and mining applications. Nezhad *et al.* (2018) presented a modeling framework for simulation of crack propagation in heterogeneous shale rocks since the understanding of the effects of the mechanical properties on both direction of cracks and rock strength is very significant. In some practical engineering, there is water or other fillers in the karst cavity which will produce cavity pressure to the surrounding rock mass. When the horizontal rock layers between tunnel and karst cave is very thin during the deep tunnel excavation, the local failure of the rock mass around the tunnel and cave will occur due to the excavation-induced stress disturbance (Zhang and Lu 2018, Huang and Zhang 2018, Pan and Dias 2018). In some cases, the pressures by fillers are very big, the fillers and rock mass will blow out (breaking into the tunnel). If the pressures are very small, the local collapse around the tunnel base will be occurred. In practical engineering, it is difficult to obtain the monitoring data about the surrounding rock collapse caused by the karst cavity pressure since when the collapse occurs the construction workers must evacuate for safety. Indeed, the progressive failure analysis leading to ultimate failure is a complicated task. Therefore, the mathematical analysis approach and optimization tool are good choices for providing guides for engineer to predict the movement trend of the failure rock mass and prevent the potential failure.

Since the karst caves exist in rich-water area, the horizontal rock layers instability exerted by disturbance stress and seepage stress cannot be ignored. The failure of the horizontal rock layers is the process of rock mass catastrophic destabilization induced by nonlinear extension of plastic zones in the horizontal rock layers. Similar to the occurrence of the collapse for the karst cave, the sinkholes formed from the sudden collapse of underground cavity are common in limestone areas. Therefore, the stability of lined tunnels in rigid plastic karst rock with supporting pressure is a problem with similar boundary conditions as the karst rock dome. Inspired by this assumption, this work used upper bound theory to characterize the failure shape of karst cave beneath the deep tunnels with the calculus of variations and modified Hoek-Brown failure criterion, which has similarity to the collapse mechanism of shallow tunnel by Luo and Yang (2018).

In this study, the author will set active and passive modes to describe the movements of potential failure blocks depending on the range of karst cavity pressure produced by fillers (Fig. 1). Both 2D and 3D failure mechanisms of the ellipsoidal cavity are put forward to describe the failure patterns of the horizontal rock layers. By considering the

*Corresponding author, Ph.D. Student
E-mail: rzhang32@sheffield.ac.uk
[a]Professor
E-mail: yangky@aliyun.com

ISSN: 2005-307X (Print), 2092-6219 (Online)

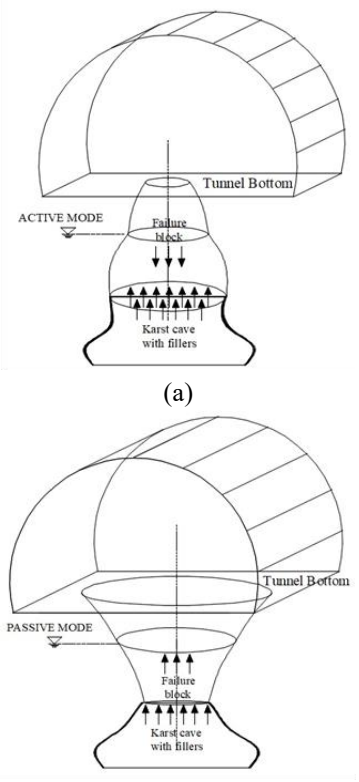

Fig. 1 Failure mechanism predictions of a karst cave beneath a tunnel: (a) active case and (b) passive case

fact that the stability of horizontal rock layers in water-rich area is affected by the seepage forces, this work discusses the effects of varying water level on the failure patterns of horizontal rock layers. The changing laws of the scope of the failure pattern obtained in this work show good consistency with the fact and previous published work.

2. General method of analysis

2.1 Theory framework

In this work the kinematically velocity field is admissible and useful for the derivation of upper bound solutions (Chen 1975, Qin and Chian 2017, Xu *et al.* 2018, Zhu and Yang, 2018). To evaluate stability of the rock mass around the cavity beneath the deep tunnel, a suitable failure criterion is essential. Since the relationships between shear stress and normal stress for rock mass tend to be nonlinear, the failure criterion adopted here is the nonlinear modified Hoek-Brown (HB) criterion (Hoek & Brown 1980, 1997). It is well known that the nonlinear Hoek-Brown (HB) criterion is written in the σ_1–σ_3 plane, but the strength of rock mass is determined by normal and shear stresses. Based on the efforts of Hoek and Brown (1997), the original form of HB rule expressed in the σ_1–σ_3 plane has been converted to power-type form in the Mohr's plane σ_n–τ.

$$\tau = A\sigma_{ci}[(\sigma_n - \sigma_{tm}) / \sigma_{ci}]^B \tag{1}$$

where σ_n and τ are normal and shear stresses on the failure surface, respectively; A and B are material constants, σ_{ci} is the uniaxial compressive strength, σ_{tm} is axial tensile stress. The details of how are the constants A and B appearing in Eq. (1) related to the modified HB criterion constants (m, s, a) are demonstrated by Hoek and Brown (1997).

The failure discontinuity layout should satisfy the velocity boundary condition and the compatibility between the strain rates and velocity according to the limit analysis theory. The set of formulations of this problem applies to a translational failure mode in the following.

2.2 Upper bound analysis

The upper bound theorem of limit analysis can be depicted as: when the velocity boundary conditions and consistency conditions for strain and velocity are satisfied by the kinematically admissible velocity field, the actual loads should be less than the calculated loads derived from equating the rate of external work to the energy dissipation rate. According to the literature (Chen 1975, Li and Yang 2018a, b), the upper bound theorem can be written as follows

$$\int_V \sigma_{ij} \cdot \dot{\varepsilon}_{ij} dV \geq \int_S P_i \cdot v_i dS + \int_V X_i \cdot v_i dV \tag{2}$$

where σ_{ij} is the stress tensor, $\dot{\varepsilon}_{ij}$ is the strain rate in velocity field. P_i is the limit load exerted on the boundary surface. S is the length of velocity discontinuity, X_i is the body force, V is the volume of the plastic zone, v_i is the velocity along the velocity discontinuity.

The upper bound procedure requires that the external work rate be equated to the energy dissipation rate within the plastic zone (Li and Yang 2019, Yang and Chen 2019, Yang and Zhang 2019, Zhang and Smith 2019, Zhang and Yang 2019, Zhang *et al.* 2019). This requires (Baker and Frydman 1983)

$$W_{ex}(P, \beta_i) = W_D(\beta_i) \tag{3}$$

where W_{ex}= external work rate, P = limit load, β_i= a set of geometrical parameters defining the failure mechanism, and W_D= energy dissipation rate.

2.3 Kinematic constraints

Since the aim of this work is to investigate the kinematic analysis of the impending failure block, the attention should be focused on the admissible velocity fields, v, which are assumed in the direction of the z-axis, as shown in Figs. 2 and 3. Compared with limit equilibrium approach which does not account for the kinematic requirements, limit analysis method used in this work is a rigorous and concise theoretical method. In kinematic analysis, the compatibility between the strain rates and velocity is satisfied as below.

By assuming the plastic potential, Ψ, to be coincident with the Mohr envelope and considering without any loss of generality, τ is positive, it is

$$\Psi = \tau - A\sigma_{ci}\left(\frac{\sigma_n - \sigma_{tm}}{\sigma_{ci}}\right)^B \tag{4}$$

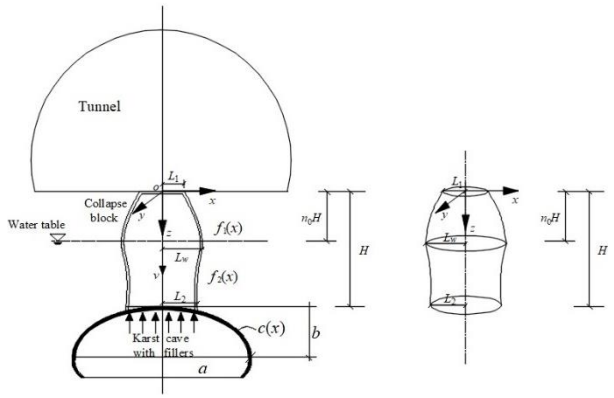

Fig. 2 Active failure mechanism of a karst cave beneath a tunnel

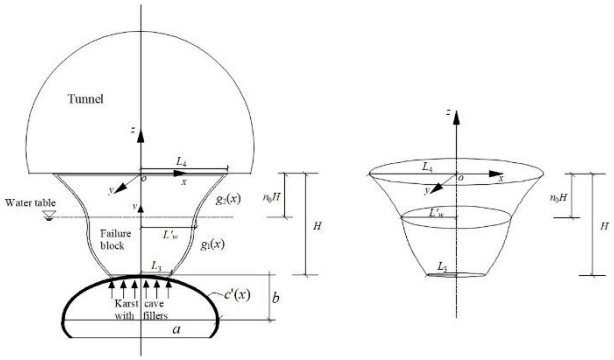

Fig. 3 Passive failure mechanism of a karst cave beneath a tunnel

So that the plastic strain rate can be written as follows

$$\dot{\varepsilon}_n = \lambda \frac{\partial \Psi}{\partial \sigma_n} = -\lambda AB \left(\frac{\sigma_n - \sigma_{tm}}{\sigma_{ci}} \right)^{B-1} \tag{5a}$$

$$\dot{\gamma}_n = \lambda \frac{\partial \Psi}{\partial \tau} = \lambda \tag{5b}$$

where λ is a scalar parameter. As shown in Fig. 2, the plastic strain rate components can be written in the form (Zhang and Yang 2018)

$$\dot{\varepsilon}_n = -\frac{v}{t}\left[1+ f'(x)^2\right]^{-\frac{1}{2}} \tag{6a}$$

$$\dot{\gamma}_n = \frac{v}{t} f'(x)\left[1+ f'(x)^2\right]^{-\frac{1}{2}} \tag{6b}$$

The scalar parameter λ can be expressed as

$$\lambda = \frac{v}{t} f'(x)\left[1+ f'(x)^2\right]^{-\frac{1}{2}} \tag{7}$$

where t is the thickness of the plastic detaching zone.

3. Active and passive failure modes with pore-water pressure

Based on previous analysis, a new failure mechanism is put forward. According to Figs. 2 and 3, two failure shape curves are adopted to reflect the different failure mechanisms of rock mass up and down the water level due to the fact that the water level will change during the excavation of deep tunnels and progressive failure of cavity. The karst cavity is embedded within ideally plastic homogeneous rock with depth H. Numerous cavities tend to have rectangular, circular, or other arched shape profiles (Luo and Yang 2018). This work adopts elliptical cross section which is determined by geometry coefficients a and b. The horizontal semiaxis of elliptical profile a stands for the cavity span, while the vertical semiaxis b is the ceiling height.

With reference to Figs.2 and 3, it results,

$$\int_0^{L_2} c(x)dx = (H+b)L_2 - \frac{b}{2a}\left(L_2^{\,2}\sqrt{a^2 - L_2^{\,2}} + \frac{a^2}{2}\arcsin\frac{L_2}{a} \right) \tag{8}$$

$$\int_0^{L_3} c'(x)dx = -(H+b)L_3 + \frac{b}{2a}\left(L_3^{\,2}\sqrt{a^2 - L_3^{\,2}} + \frac{a^2}{2}\arcsin\frac{L_3}{a} \right) \tag{9}$$

In terms of the direction of the failure pattern movements, analytical expressions for failure surfaces are derived in the following.

3.1 Collapse active failure mechanism

The active failure mechanism for karst cavity is shown in Fig. 2. Within the framework of upper bound theorem, the energy dissipation occurs only along the slip-line. Based on the work of Fraldi and Guarracino (2010) and Sun *et al.* (2018), the dissipation density of a random point could be as,

$$\dot{D}_i = \sigma_n \cdot \dot{\varepsilon}_n + \tau \cdot \dot{\gamma}_n = \frac{v}{t}\left[1+ f'(x)^2\right]^{-\frac{1}{2}}\left[\sigma_{tm} - \sigma_{ci}\left[ABf'(x)\right]^{\frac{1}{1-B}}(1-B^{-1}) \right] \tag{10}$$

In active mechanism, the energy dissipation along the velocity discontinuity surface can be obtained by integrating $\dot{D}_i$ over the interval $[L_1, L_2]$,

$$\begin{aligned} W_D = &\int_{L_1}^{L_w} \left\{ \sigma_{tm1} - \sigma_{ci1}\left[A_1 B_1 f_1'(x)\right]^{\frac{1}{1-B_1}}(1-B_1^{-1}) \right\} v dx \\ &+ \int_{L_w}^{L_2} \left\{ \sigma_{tm1} - \sigma_{ci1}\left[A_1 B_1 f_2'(x)\right]^{\frac{1}{1-B_1}}(1-B_1^{-1}) \right\} v dx \end{aligned} \tag{11}$$

where L_1 and L_2 are upper and lower half widths of the failure block, respectively. L_w is half width of the failure block at water level.

The work rate of the failure block produced by weight can be calculated by integral process

$$W_\gamma = v\int_0^{L_2} \gamma_1' \cdot c(x)dx - v\int_{L_w}^{L_2} \gamma_1' \cdot f_2(x)dx - v\int_{L_1}^{L_w} \gamma_1 \cdot f_1(x)dx + v\gamma_w L_w f_1(L_w) \tag{12}$$

in which γ'_1 is the buoyant weight per unit volume of the rock mass. $\gamma'_1=\gamma_1-\gamma_w$, where γ_1 is the weight per unit volume of the rock mass, and γ_w is the unit weight of water. $c(x)$ is the profile of cavity in active failure mode.

The distribution of excess pore pressure which is derived from the study of Saada *et al.* (2012) can be written

as

$$u = p - p_w = p - \gamma_w h_w \tag{13}$$

where p is the pore water pressure at the considered point which can be obtained by a suitable method $p=r_u\gamma h_w$, r_u stands for pore pressure coefficient, and $p_w=\gamma_w h_w$ is the hydrostatic distribution for pore pressure, h_w is the vertical distance between the tunnel base and the bottom of the failure block. So -*grad u* can be defined as

$$-grad\ u = \gamma_w - r_u\gamma \tag{14}$$

The explicit form of the work rate of the seepage force is,

$$W_u = v\int_0^{L_w}(\gamma_w - r_u\gamma_1)\cdot[c(x) - f_2(L_w)]dx - v\int_{L_w}^{L_2}(\gamma_w - r_u\gamma_1)\cdot[f_2(x) - f_2(L_w)]dx \tag{15}$$

As mentioned above, the limit load in dimensionless form could be given by

$$N_\gamma = q/\gamma H \tag{16}$$

where N_γ is analogous to the stability factor. Then, based on Eq.(3),

$$\begin{aligned} N_\gamma &= \left(W_D - W_\gamma - W_u\right)/v\gamma_1 HL_2 \\ &= \left\{\int_{L_1}^{L_w}\psi_1[f_1(x), f_1'(x), x]dx + \int_{L_w}^{L_2}\psi_2[f_2(x), f_2'(x), x]dx \right. \\ &\quad \left. +(r_u\gamma_1 - \gamma_1)\int_0^{L_2}c(x)dx - r_u\gamma_1 L_w f_1(L_w)\right\}/\gamma_1 HL_2 \end{aligned} \tag{17}$$

in which

$$\psi_1[f_1(x), f_1'(x), x] = \sigma_{tm1} - \sigma_{ci1}\left[A_1B_1 f_1'(x)\right]^{\frac{1}{1-B_1}}(1 - B_1^{-1}) + \gamma_1 f_1(x) \tag{18a}$$

$$\psi_2[f_2(x), f_2'(x), x] = \sigma_{tm1} - \sigma_{ci1}\left[A_1B_1 f_2'(x)\right]^{\frac{1}{1-B_1}}(1 - B_1^{-1}) + (1 - r_u)\gamma_1 f_2(x) \tag{18b}$$

By virtue of the Greenberg minimum principle, the optimal failure mechanism can be obtained with stationary requirement, which may be expressed by the following Euler equation

$$\partial G[f(x), f'(x), x] = 0 \Rightarrow \frac{\partial\psi}{\partial f(x)} - \frac{\partial}{\partial x}\left[\frac{\partial\psi}{\partial f'(x)}\right] = 0 \tag{19}$$

The explicit form of the Euler's equation for the Eq. (19) can be obtained as

$$1 - \frac{\sigma_{ci1}}{\gamma_1}(A_1B_1)^{\frac{1}{1-B_1}}\left[f_1'(x)\right]^{\frac{2B_1-1}{1-B_1}}(1 - B_1)^{-1} f_1''(x) = 0 \tag{20a}$$

$$1 - r_u - \frac{\sigma_{ci1}}{\gamma_1}(A_1B_1)^{\frac{1}{1-B_1}}\left[f_2'(x)\right]^{\frac{2B_1-1}{1-B_1}}(1 - B_1)^{-1} f_2''(x) = 0 \tag{20b}$$

Integration of nonlinear second-order homogeneous differential equation Eq. (20) gives the expression of failure surface,

$$f_1(x) = k_1(x - \frac{c_0}{\gamma_1})^{\frac{1}{B_1}} + c_1 \tag{21a}$$

$$f_2(x) = k_2\left[x - \frac{c_2}{(1 - r_u)\gamma_1}\right]^{\frac{1}{B_1}} + c_3 \tag{21b}$$

where

$$k_1 = A_1^{-\frac{1}{B_1}}\left(\frac{\gamma_1}{\sigma_{ci1}}\right)^{\frac{1-B_1}{B_1}} \tag{22a}$$

$$k_2 = A_1^{-\frac{1}{B_1}}\left[\frac{(1 - r_u)\gamma_1}{\sigma_{ci1}}\right]^{\frac{1-B_1}{B_1}} \tag{22b}$$

where $c_i(i=0,1,2,3)$ stand for the integration constant coefficients determined by geometric constraints. Due to the stress equilibrium condition that the shear stress vanishes at the tunnel base, the stress condition should be satisfied,

$$\tau_{xy}(x = L_1, z = 0) = 0 \tag{23}$$

As shown in Fig. 2, the constraints should be considered

$$f_1(x = L_1) = 0 \tag{24}$$

$$f_1(x = L_w) = f_2(x = L_w) = n_0 H \tag{25}$$

$$f_2(x = L_2) = c(x = L_2) \tag{26}$$

The explicit value of n_0 is the ratio of the distance between the tunnel base and water table to the depth from the cavity to the tunnel bottom. For convenience, the feasible range for n_0 is [0,1] in this work. Considering Eqs.(23) and (25), the failure curves turn into

$$f_1(x) = A_1^{-\frac{1}{B_1}}\left(\frac{\gamma_1}{\sigma_{ci1}}\right)^{\frac{1-B_1}{B_1}}(x - L_1)^{\frac{1}{B_1}} \tag{27}$$

$$c_3 = n_0 H - k_2\left[L_w - \frac{c_2}{(1 - r_u)\gamma_1}\right]^{\frac{1}{B_1}} \tag{28}$$

L_1 can be expressed by L_w based on Eqs. (25) and (27) above. The entire failure surface could be regarded as smooth in practical engineering, so the constraint should be considered.

$$f_1'(x = L_w) = f_2'(x = L_w) \tag{29}$$

Then,

$$f_2(x) = k_2(x - Z)^{\frac{1}{B_1}} - k_2(L_w - Z)^{\frac{1}{B_1}} + n_0 H \tag{30}$$

where

$$Z = L_w - \frac{L_w - L_1}{1 - r_u} \tag{31}$$

$$\begin{aligned} N_\gamma = &\left\{\left[\sigma_{tm1} - (1 - r_u)\gamma_1 k_2(L_w - Z)^{\frac{1}{B_1}} + n_0 H(1 - r_u)\gamma_1\right](L_2 - L_w)\right. \\ &+\frac{\sigma_{ci1}}{1 + B_1}\left(\frac{\gamma_1}{A_1\sigma_{ci1}}\right)^{\frac{1}{B_1}}(L_w - L_1)^{\frac{1+B_1}{B_1}} + (r_u\gamma_1 - \gamma_1)\int_0^{L_2}c(x)dx - r_u\gamma_1 L_w f_1(L_w) \\ &\left.+\frac{\sigma_{ci1}}{1 + B_1}\left[\frac{(1 - r_u)\gamma_1}{A_1\sigma_{ci1}}\right]^{\frac{1}{B_1}}\left[(L_2 - Z)^{\frac{1+B_1}{B_1}} - (L_w - Z)^{\frac{1+B_1}{B_1}}\right] + \sigma_{tm1}(L_w - L_1)\right\}/\gamma_1 HL_2 \end{aligned} \tag{32}$$

During the derivation of expressions of failure surface $f_1(x)$ and $f_2(x)$, the values of L_w and L_2 would be calculated first by solving Eqs. (26) and (32). This process is carried out numerically using MATLAB. Based on the previous analysis, when the optimal stability factor continues increasing, the cavity pressure is big enough to resist the self-weight of failure rock mass (leading to the passive failure mechanism).

3.2 Breakout passive failure mechanism

When the force produced by fillers is huge, the failure block above the cavity will break out into tunnel base. For the sake of describing the failure profile of the passive mode, similar to active mechanism, the analytical expressions should be derived, as shown in Fig. 3. L_3 and L_4 are lower and upper half widths of the failure block, respectively. L'_w is half width of the failure block at water table. $c'(x)$ is the profile of cavity in passive failure mechanism.

In passive mode Eq. (17) should take the form,

$$N_\gamma = \left\{ \int_{L_3}^{L'_w} \psi_3[g_1(x), g'_1(x), x]dx + \int_{L'_w}^{L_4} \psi_4[g_2(x), g'_2(x), x]dx + (r_u\gamma_2 - \gamma_2)\int_0^{L_3} c'(x)dx - r_u\gamma_2 L'_w g_2(L'_w) \right\} \Big/ \gamma_2 H L_3 \tag{33}$$

in which

$$\psi_3[g_1(x), g'_1(x), x] = \sigma_{tm2} - \sigma_{ci2}\left[A_2 B_2 g'_1(x)\right]^{\frac{1}{1-B_2}}(1 - B_2^{-1}) - \gamma_2(1 - r_u)g_1(x) \tag{34a}$$

$$\psi_4[g_2(x), g'_2(x), x] = \sigma_{tm2} - \sigma_{ci2}\left[A_2 B_2 g'_2(x)\right]^{\frac{1}{1-B_2}}(1 - B_2^{-1}) - \gamma_2 g_2(x) \tag{34b}$$

As shown in Fig. 3, the boundary conditions should be obtained

$$\tau_{xy}(x = L_4, z = 0) = 0 \tag{35}$$

$$g_2(x = L_4) = 0 \tag{36}$$

$$g_1(x = L'_w) = g_2(x = L'_w) = -n_0 H \tag{37}$$

$$g_1(x = L_3) = c'(x = L_3) \tag{38}$$

$$g_1'(x = L'_w) = g_2'(x = L'_w) \tag{39}$$

Therefore, the failure surfaces could be expresses as based on the above constraints,

$$g_1(x) = -k_3(Z' - x)^{\frac{1}{B_2}} + k_3(Z' - L'_w)^{\frac{1}{B_2}} - n_0 H \tag{40}$$

$$g_2(x) = -k_4(L_4 - x)^{\frac{1}{B_2}} \tag{41}$$

where

$$Z' = L'_w + \frac{L_4 - L'_w}{1 - r_u} \tag{42}$$

$$k_3 = A_2^{-\frac{1}{B_2}}\left[\frac{(1 - r_u)\gamma_2}{\sigma_{ci2}}\right]^{\frac{1-B_2}{B_2}} \tag{43}$$

$$k_4 = A_2^{-\frac{1}{B_2}}\left(\frac{\gamma_2}{\sigma_{ci2}}\right)^{\frac{1-B_2}{B_2}} \tag{44}$$

Then the objective (for stability factor) in optimization is

$$N_\gamma = \left\{ \sigma_{tm2}(L_4 - L'_w) + \left[\sigma_{tm2} - (1 - r_u)\gamma_2 k_3 (Z' - L'_w)^{\frac{1}{B_1}} + n_0 H(1 - r_u)\gamma_2\right](L'_w - L_3) + \frac{\sigma_{ci2}}{1 + B_2}\left(\frac{\gamma_2}{A_2\sigma_{ci2}}\right)^{\frac{1}{B_2}}(L_4 - L'_w)^{\frac{1+B_2}{B_2}} + (r_u\gamma_2 - \gamma_2)\int_0^{L_3} c'(x)dx - r_u\gamma_2 L'_w g_2(L'_w) + \frac{\sigma_{ci2}}{1 + B_2}\left[\frac{(1 - r_u)\gamma_2}{A_2\sigma_{ci2}}\right]^{\frac{1}{B_2}}\left[(Z' - L_3)^{\frac{1+B_2}{B_2}} - (Z' - L'_w)^{\frac{1+B_2}{B_2}}\right] \right\} \Big/ \gamma_2 H L_3 \tag{45}$$

L_4 can be expressed by L'_w based on Eqs. (37) and (41) above. And the values of L'_w and L_3 would be calculated by solving Eqs. (38) and (45).

4. Three dimensional failure mechanism analysis

Normally the failure surface of the horizontal rock layers is assumed in the form of the frustum of a cone in three-dimensional space. In this work, the plane strain failure mechanism of karst cavity roof could be extended to the axisymmetric failure mechanism in practical engineering by rotating the two-dimensional plane-strain curved surface around the *z*-axis, as shown in Figs. 2 and 3. An axisymmetric failure mechanism (by rotating two-dimensional plane failure surface 360° around the *z*-axis) is suitable to describe the failure profile since this agrees well with the fact.

For active mechanism in 3D space, the energy dissipation along the velocity discontinuity surface can be obtained,

$$W_D = 2\pi\int_{L_1}^{L_w}\left\{\sigma_{tm3} - \sigma_{ci3}\left[A_3 B_3 f'_1(x)\right]^{\frac{1}{1-B_3}}(1 - B_3^{-1})\right\}xvdx + 2\pi\int_{L_w}^{L_2}\left\{\sigma_{tm4} - \sigma_{ci4}\left[A_4 B_4 f'_2(x)\right]^{\frac{1}{1-B_4}}(1 - B_4^{-1})\right\}xvdx \tag{46}$$

where σ_{tm3}, σ_{ci3}, A_3 and B_3 are the mechanical parameters of the upper rock stratum in active failure mode, σ_{tm4}, σ_{ci4}, A_4 and B_4 are the mechanical parameters of the lower rock stratum in active failure mode.

The work rate of the failure block produced by weight can be calculated by integral process

$$W_\gamma = -v\pi\int_{L_w}^{L_2}\gamma_4 \cdot f'_2(x)x^2dx - v\pi\int_{L_1}^{L_w}\gamma_3 \cdot f'_1(x)x^2dx \tag{47}$$

where γ_3 and γ_4 are the self-weight density of the upper rock stratum and lower rock stratum in active failure, respectively. The explicit form of the work rate of the seepage force is,

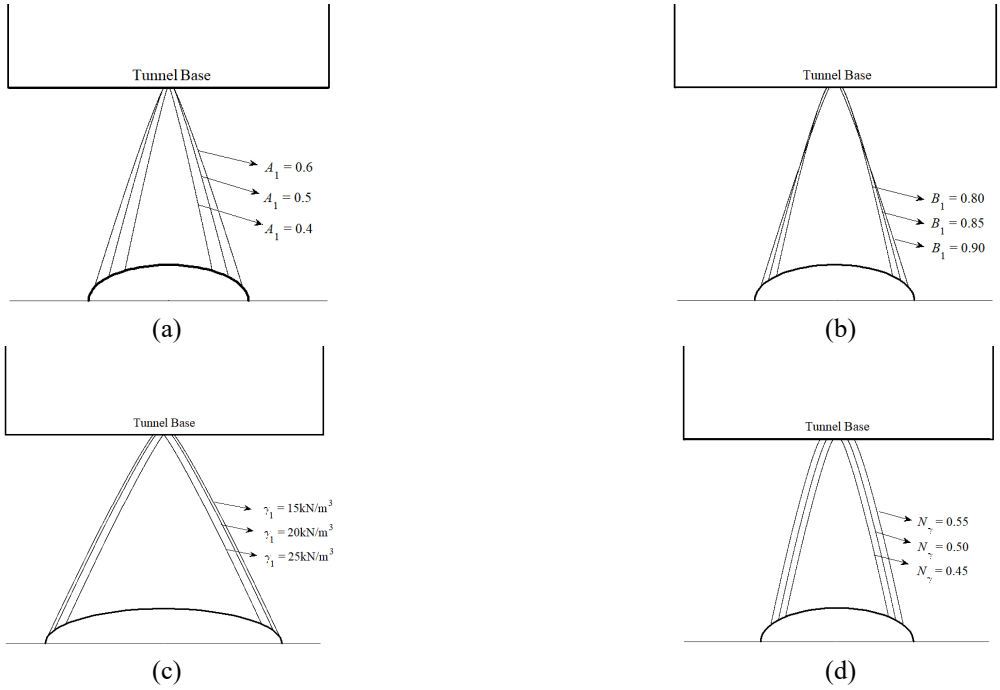

Fig.4. Predictions for active failure scope of horizontal rock layers for different parameters: (a) different A_1, (b) different B_1, (c) different γ_1 and (d) different $N\gamma$

$$W_u = 2\pi v\int_{L_w}^{L_2} r_u\gamma_4\cdot\left[f_2(x)+1-n_0H\right]xdx \tag{48}$$

The work rate of the cavity pressure is,

$$W_q = \pi L_2^2 q \tag{49}$$

By variational method, the expressions of failure surfaces could be derived with undetermined parameters. The explicit expressions of failure surfaces can be obtained based on the boundary condition below,

$$\tau_{xy}(x=L_1, z=0)=0 \tag{50a}$$

$$f_1(x=L_1)=0 \tag{50b}$$

$$f_1(x=L_2)=H \tag{50c}$$

Similar to the active failure mechanism analysis, the expressions of passive failure surfaces could be derived with variation calculus. The three-dimensional failure mechanism can be obtained by rotating two-dimensional plane passive failure surface 360° around the z-axis.

5. Sensitivity analysis

5.1 Effects of parameters on failure mechanism

If the potential failure region can be predicted, proper reinforcement measures can be taken by geotechnical engineers to make the construction safe. To determine the sensitivity of scope of failure pattern to rock properties and cavity pressure, parametric analysis is conducted to elucidate the influence of various factors on potential failure range in two-dimensional space. The failure surfaces in two-dimensional space for different rock parameters and cavity pressure corresponding to B=0.80-0.90, A=0.4-0.6, σ_{ci}=10 MPa, n_0=0, r_u=0, σ_{tm}=σ_{ci}/100, γ=15-25 kN/m^3, b=1 m, a=3 m, H= 5 m, and Nγ=0.45-0.55 are illustrated in Fig. 4.

It can be seen that the failure profile extends from the roof of the karst cave to the tunnel base, the range of the failure surface is influenced by different rock parameters B, A, γ and $N\gamma$. The range of the failure surface increases with increase of B and A, but decreases with increase of γ both in active and passive mechanism. Since the 3D failure mechanism is built based on the 2D failure mechanism (just built by rotating two-dimensional plane failure surface 360° around the z-axis), the changing laws in 3D mechanism should be as the same as those in the 2D mechanism. From a practical viewpoint, the surrounding rock mass with lower values of B and A and higher value of γ will contribute to reducing the scope of the failure pattern.

5.2 Effects of pore-water pressure on failure mechanism

The groundwater levels in karst areas play a significant role in determining the failure mechanism of the horizontal rock layers. According to Fig. 5, the upper and lower widths of the failure rock block in two-dimensional space (corresponding to B=0.80, A=0.6, σ_{ci}=10 MPa, σ_{tm}=σ_{ci}/100, γ=25 kN/m^3, b= 1 m, a=3 m, H=5 m, and Nγ=0.55) L_1 and L_2 both decrease with the increase of n_0 in active mode. But in two-dimensional passive case the lower and upper widths of the failure rock block L_3 and L_4 both increase with the increase of n_0. This finding shows good consistency with

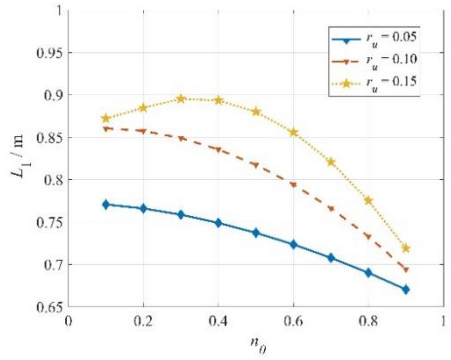

(a) Effects on upper half widths of the failure block L_1

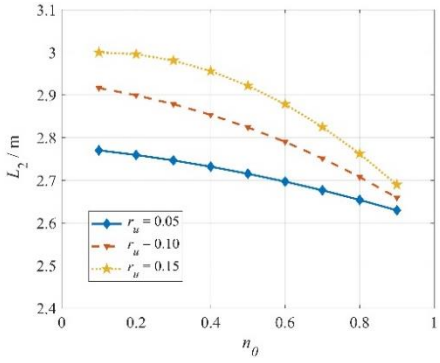

(b) Effects on lower half widths of the failure block L_2

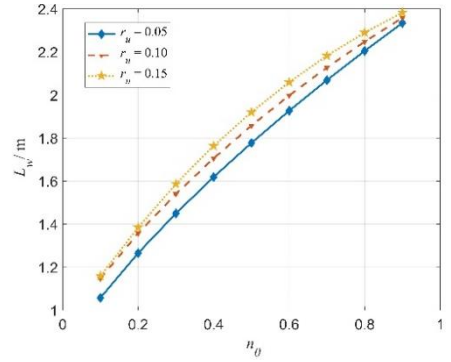

(c) Effects on half width of the failure block at water level L_w

Fig. 5 Effects of pore-water pressure coefficient r_u on scope of failure pattern in active mechanism

Table 1 Effects of varying water level and pore pressure coefficient on active failure scopes in 3D space

A_3	A_4	B_3	B_4	γ_3 (kN/m^3)	γ_4 (kN/m^3)	σ_{c3} (MPa)	σ_{c4} (MPa)	r_u	n_0	L_w(m)	L_2(m)
0.3	0.5	0.8	0.7	20	25	1	1.5	0.2	0.3	0.47	2.87
0.3	0.5	0.8	0.7	20	25	1	1.5	0.2	0.5	0.85	2.86
0.3	0.5	0.8	0.7	20	25	1	1.5	0.2	0.7	1.29	2.68
0.3	0.5	0.8	0.7	20	25	1	1.5	0.0	0.5	1.05	3.29
0.3	0.5	0.8	0.7	20	25	1	1.5	0.1	0.5	0.94	3.04
0.3	0.5	0.8	0.7	20	25	1	1.5	0.2	0.5	0.85	2.86

the fact that collapse is more likely to occur under larger seepage forces (pore water pressure) in active mode. By considering the critical state for L_1=0, the effects of varying water level and pore pressure coefficient on active failure scopes in 3D space is shown in Table.1.

From a practical viewpoint, the horizontal rock layers with lower value of r_u and higher value of n_0 will contribute to reducing the scope of the failure pattern in active mechanism; the horizontal rock layers with higher value of r_u and lower value of n_0 will contribute to reducing the scope of the failure pattern in passive mechanism.

6. Conclusions

In this study, both active and passive collapse shapes of rock mass above the karst cavity is put forward when the surrounding rock cannot bear the pressure caused by the concealed cavity. Depending on the range of cavity pressure of fillers in cave, different failure modes are put forward in non-linear horizontal rock layers determining by modified HB failure criterion. Within the framework of upper bound theory, a new convenient way to include seepage effects is also presented and implemented, which can be used to explain the changing laws for scopes of failure patterns with varying water level and pore pressure coefficients. The main research findings include:

• Both 2D and 3D failure mechanisms are put forward to describe the failure patterns of the horizontal rock layers with considering the varying water level.

• The scope of the failure surface is influenced by different rock parameters B, A and γ. The range of the failure surface increases with increase of B and A, but decreases with increase of γ both in active and passive mechanism.

• The horizontal rock layers with lower value of r_u and higher value of n_0 will contribute to reducing the scope of the failure pattern in active mechanism; the horizontal rock layers with higher value of r_u and lower value of n_0 will contribute to reducing the scope of the failure pattern in passive mechanism. This conclusion agrees well with the fact that collapse is more likely to occur under larger seepage forces (pore water pressure) in active mode, which is a validation of this study.

References

Baker, R. and Frydman, S. (1983), "Upper bound limit analysis of soil with non-linear failure criterion", *Soil. Found.*, **23**, 34-42. https://doi.org/10.3208/sandf1972.23.4_34.

Chen, W.F. (1975), *Limit Analysis and Soil Plasticity*, Elsevier Science, Amsterdam, The Netherlands.

Daraei, A. and Zare, S. (2018), "A new strain-based criterion for evaluating tunnel stability", *Geomech. Eng.*, **16**(2), 205-215. https://doi.org/10.12989/gae.2018.16.2.205.

Fraldi, M. and Guarracino, F. (2010), "Analytical solutions for collapse mechanisms in tunnels with arbitrary cross sections", *Int. J. Solid Struct.*, **47**(2), 216-223. https://doi.org/10.1016/j.ijsolstr.2009.09.028.

Hoek, E. and Brown, E.T. (1997), "Practical estimates of rock mass strength", *Int. J. Rock Mech. Min. Sci.*, **34**(8), 1165-1186. https://doi.org/10.1016/S1365-1609(97)80069-X.

Hoek, E. and Brown, E.T. (1980), Underground excavations in rock. London: Institute of Mining and Metallurgy.

Huang, X.L and Zhang, R. (2018), "Catastrophe stability analysis for shallow tunnels considering settlement", *J. Cent. South Univ.*, **25**(4), 949-960. https://doi.org/10.1007/s11771-018-3796-6.

Li, T.Z. and Yang, X.L. (2018a), "Probabilistic stability analysis of

subway tunnels combining multiple failure mechanisms and response surface method", *Int. J. Geomech*., **18**(12), 04018167. https://doi.org/10.1061/(ASCE)GM.1943-5622.0001315.
Li, Y.X. and Yang, X.L. (2019), "Seismic displacement of 3D slope reinforced by piles with nonlinear failure criterion", *Int. J. Geomech*.„ **19**(6), 04019042. https://doi.org/10.1061/(ASCE)GM.1943-5622.0001411.
Li, Z.W. and Yang, X.L. (2018b), "Active earth pressure for soils with tension cracks under steady unsaturated flow conditions", *Can. Geotech. J*., **55**(12),1850-1859. https://doi.org/10.1139/cgj-2017-0713.
Lin, P., Li, S.C., Xu, Z.H., Huang, X., Pang, D.D., Wang, X.T. and Wang, J. (2018), "Location determining method of critical sliding surface of fillings in a karst cave of tunnel", *Geomech. Eng*., **16**(4), 415-421. https://doi.org/10.12989/gae.2018.16.4.415.
Luo, W.J. and Yang, X.L. (2018), "3D stability of shallow cavity roof with arbitrary profile under influence of pore water pressure", *Geomech. Eng*.,**16**(6), 569-575. https://doi.org/10.12989/gae.2018.16.6.569.
Nezhad, M.M., Fisher, Q.J., Gironacci, E. and Rezania, M. (2018), "Experimental study and numerical modeling of fracture propagation in shale rocks during Brazilian disk test", *Rock Mech. Rock Eng*., **51**(6), 1755-1775. https://doi.org/10.1007/s00603-018-1429-x.
Nezhad, M.M., Gironacci, E., Rezania, M. and Khalili, N. (2018), "Stochastic modelling of crack propagation in materials with random properties using isometric mapping for dimensionality reduction of nonlinear data sets", *Int. J. Numer. Meth. Eng*., **113**(4), 656-680. https://doi.org/10.1002/nme.5630.
Pan, Q. and Dias, D. (2018), "Three dimensional face stability of a tunnel in weak rock masses subjected to seepage forces", *Tunn. Undergr. Sp. Technol*., **71**, .555-566. https://doi.org/10.1016/j.tust.2017.11.003.
Qin, C.B. and Chian, S.C. (2017), "Kinematic analysis of seismic slope stability with a discretisation technique and pseudo-dynamic approach: a new perspective", *Geotechnique*, **68**(6), 492-503. https://doi.org/10.1680/jgeot.16.P.200.
Saada, Z., Maghous, S. and Garnier, D. (2012), "Stability analysis of rock slopes subjected to seepage forces using the modified Hoek-Brown criterion", *Int. J. Rock Mech. Min. Sci*., **55**(1), 45-54. https://doi.org/10.1016/j.ijrmms.2012.06.010.
Sahoo, J.P. and Kumar, J. (2018), "Required Lining Pressure for the stability of twin circular tunnels in soils", *Int. J. Geomech*., **18**(7), 04018069. https://doi.org/10.1061/(ASCE)GM.1943-5622.0001196.
Sun, Z.B., Li, J., Pan, Q.J., Dias, D., Li, S. and Hou, C. (2018), "Discrete kinematic mechanism for nonhomogeneous slopes and its application", *Int. J. Geomech*., **18**(12), 04018171. https://doi.org/10.1061/(ASCE)GM.1943-5622.0001303.
Xu, J.S., Li, Y.X. and Yang, X.L. (2018), "Seismic and static 3D stability of two-stage slope considering joined influences of nonlinearity and dilatancy", *KSCE J. Civ. Eng*., **22**(10), 3827-3836. https://doi.org/10.1007/s12205-018-0636-z.
Yang, X.L. and Chen, J.H. (2019), "Factor of safety of geosynthetic-reinforced slope in unsaturated soils", *Int. J. Geomech*., **19**(6), 04019041. https://doi.org/10.1061/(ASCE)GM.1943-5622.0001399.
Yang, X.L. and Zhang, S. (2019), "Seismic active earth pressure for soils with tension cracks", *Int. J. Geomech*., **19**(6), 06019009. https://doi.org/10.1061/(ASCE)GM.1943-5622.0001414.
Zhang, D.B., Jiang Y. and Yang, X.L. (2019), "Estimation of 3D active earth pressure under nonlinear strength condition", *Geomech. Eng*., **17**(6), 515-525. https://doi.org/10.12989/gae.2019.17.6.569.
Zhang, R. and Lu, S.P. (2018), "Kinematic analysis of shallow tunnel in layered strata considering joined effects of settlement and seepage", *J. Cent. South Univ*., **25**(2), 368-378. https://doi.org/10.1007/s11771-018-3743-6.
Zhang, R. and Smith, C.C. (2019), "Upper bound limit analysis of soils with a non-linear failure criterion", *Can. Geotech. J*., https://doi.org/10.1139/cgj-2018-0513.
Zhang, R. and Yang, X.L. (2018), "Limit analysis of active and passive mechanisms of shallow tunnels in nonassociative soil with changing water table", *Int. J. Geomech*., **18**(7), 04018063. https://doi.org/10.1061/(ASCE)GM.1943-5622.0001167.
Zhang, R. and Yang, X.L. (2019), "Limit analysis of anchor trapdoor embedded in nonhomogeneous and nonlinear soils", *Int. J. Geomech*. https://doi.org/10.1061/(ASCE)GM.1943-5622.0001476.
Zhu, J.Q. and Yang, X.L. (2018), "Probabilistic stability analysis of rock slopes with cracks", *Geomech. Eng*., **16**(6), 655-667. https://doi.org/10.12989/gae.2018.16.6.655.

JS

Nomenclature

A	Rock mass material constants
B	Rock mass material constants
σ_{ci}	Uniaxial compressive strength
σ_{tm}	Axial tensile stress
σ_n	Normal stress
τ	Shear stress
σ_{ij}	Stress tensor
$\dot{\varepsilon}_{ij}$	Strain rate
v, v_i	Velocity of the failure rigid block
P	Limit load
S	Length of velocity discontinuity
X_i	Body force
V	Volume of the plastic zone
W_{ex}	External work rate
β_i	A set of geometrical parameters defining the failure mechanism
W_D	Energy dissipation rate
$f(x)$	The function describing the failure surface in active model
W_γ	Work rate done by the body forces (self-weight)
W_u	Pore water pressure power

P_m	The minimum value of P
Ψ	Plastic potential function
λ	Scalar parameter
t	Thickness of the plastic detaching zone
$\dot{\varepsilon}_n$	Normal plastic strain rate
$\dot{\gamma}_n$	Shear plastic strain rate
$\dot{D}_i$	Dissipation rate
L_i(i=1,2,3,4)	Half width of the failure block
L_w, L'_w	Half width of the failure block at water level
N_γ	Stability factor
q	Supporting pressure
H	Embedded depth
γ	Unit weight of the rock
γ'	Buoyant unit weight of the rock
γ_w	Unit weight of water
p	Pore water pressure at the considered point
r_u	Pore pressure coefficient
p_w	Hydrostatic distribution for pore pressure
h_w	Vertical distance between the tunnel base and bottom of the failure block
$g_i(x)$ (i=1,2)	The profile of the failure surface in passive mode
$c(x)$, $c'(x)$	The profiles of the karst cavity both in active and passive mode
c_0, c_1, c_2, c_3	Constant coefficients describing the failure surface